Bioinspiration & Biomimetics

PAPER

Trout-like multifunctional piezoelectric robotic fish and energy harvester

David Tan, Yu-Cheng Wang, Eetu Kohtanen and Alper Erturk[*]

G.W. Woodruff School of Mechanical Engineering, Georgia Institute of Technology, Atlanta, GA 30332, United States of America
[*] Author to whom any correspondence should be addressed.

E-mail: alper.erturk@me.gatech.edu

Abstract

This work presents our experimental studies on a trout-inspired multifunctional robotic fish as an underwater swimmer and energy harvester. Fiber-based flexible piezoelectric composites with interdigitated electrodes, specifically macro-fiber composite (MFC) structures, strike a balance between the deformation and actuation force capabilities to generate hydrodynamic propulsion without requiring additional mechanisms for motion amplification. A pair of MFC laminates bracketing a passive fin functions like artificial muscle when driven out of phase to expand and contract on each side to create bending. The trout-like robotic fish design explored in this work was tested for both unconstrained swimming in a quiescent water tank and under imposed flow in a water tunnel to estimate the maximum swimming speed, which exceeded 0.25 m s^{-1}, i.e., 0.8 body lengths per second. Hydrodynamic thrust characterization was also performed in a quiescent water setting, revealing that the fin can easily produce tens of mN of thrust, similar to its biological counterpart for comparable swimming speeds. Overall, the prototype presented here generates thrust levels higher than other smart material-based concepts (such as soft polymeric material-based actuators which provide large deformation but low force), while offering simple design, geometric scalability, and silent operation unlike motor-based robotic fish (which often use bulky actuators and complex mechanisms). Additionally, energy harvesting experiments were performed to convert flow-induced vibrations in the wake of a cylindrical bluff body (for different diameters) in a water tunnel. The shed vortex frequency range for a set of bluff body diameters covered the first vibration mode of the tail, yielding an average electrical power of 120 μW at resonance for a flow speed around 0.3 m s^{-1} and a bluff body diameter of 28.6 mm. Such low-power electricity can find applications to power small sensors of the robotic fish in scenarios such as ecological monitoring, among others.

1. Introduction

Bioinspired robotic fish research [1] has received growing interest for various applications such as underwater ecological exploration [2] and studying fish school dynamics [3], among others. Both conventional and non-conventional actuation methods have been widely explored to enable underwater swimmer platforms [4–6]. Early efforts in the field of bioinspired underwater robotics can be traced back to the work of Triantafyllou and coworkers [7, 8], and this research domain has rapidly evolved to exhibit a plethora of design concepts spanning from motor-based actuators [4] to smart materials [6].

Since the early research in the 1990s, motor-driven robotic swimmers have undergone various developments, from improved mechanical design [9–17] to enhanced control for complex maneuvering, collision avoidance, and autonomous navigation [18–25]. Motor-based robotic fish research is relatively mature and widely used in large-scale designs. The use of multiple motors and complex mechanisms for motion transmission were historically some of their undesired characteristics. However, the domain of motor-based compliant robotic

fish [26] has evolved into successful soft-body design concepts [27, 28] with reduced number of motors and increased efficiency.

As an alternative to conventional motor-based actuator concepts, smart material-based designs [6] offer various advantages such as simple design, silent operation (without acoustic signature), and ease of small-scale fabrication. According to one definition [29], smart materials are those that exhibit coupling between multiple physical domains. In general, certain properties of smart materials can be significantly varied by changing an external stimulus (e.g., electric field, magnetic field, temperature, etc), and, in that regard, smart materials are stimuli-responsive. Various smart materials have been employed in the existing literature for bioinspired robotic fish design, such as ionic polymer–metal composites (IPMCs), shape-memory alloys (SMAs), and piezoelectric materials.
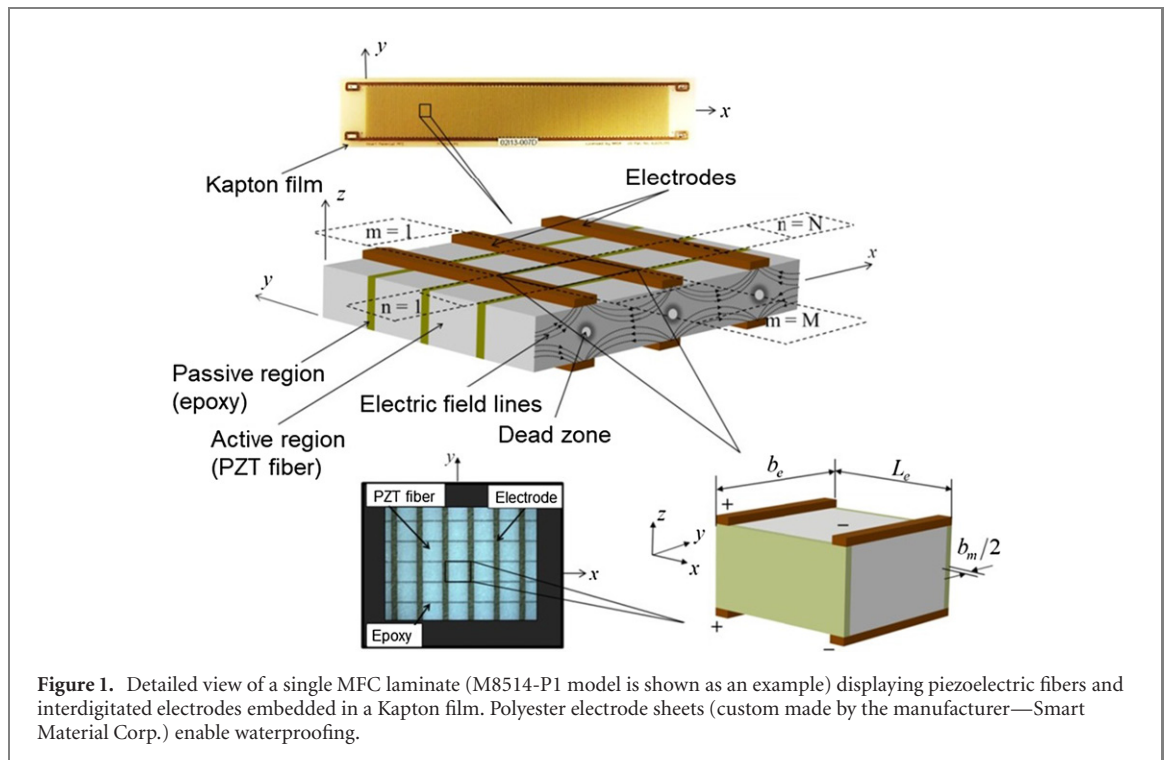
IPMCs are ionic electroactive polymers, and they are arguably the most popular smart materials used in underwater swimmer design [30–39]. IPMC materials (e.g., Nafion) are attractive for robotic fish design because their actuation mechanism resembles muscle contraction. Actuation in IPMCs is achieved by leveraging an imbalance of ions within a polymer membrane to create local swelling and shrinking of the material in response to alternating electrical input. IPMC designs exhibit large deformations, but their actuation force is relatively low, resulting in slow swimming speeds. Another class of smart materials, SMAs (e.g., nickel–titanium), provide an actuation mechanism enabled by temperature change as explored by various researchers in underwater thrust generation [40–45]. The time-dependent temperature variation needs to be large enough to create the required phase transformation within the material for high actuation levels. The need for large temperature change makes SMA-based robotic fish a relatively less explored candidate for autonomous behavior where the control of temperature may be limited. Another group of less studied smart materials for underwater robotics is piezoelectric materials (e.g., PZT: lead zirconate titanate). Piezoelectric ceramics typically provide large actuation forces but low deformation. As a result, early piezoelectric swimmer designs used motion amplification mechanisms [46–48] (to increase the deformation at the expense of reduced actuation force and added complexity as well as loss). Furthermore, piezoelectric actuation voltage levels are often high (much higher than those of IPMCs), creating additional challenges in designing battery-powered, untethered swimmers.

Fiber-based flexible piezoelectric structures with interdigitated electrodes, namely the macro-fiber composite (MFC) technology developed by the NASA Langley Research Center [49–51], emerged as an actuator alternative that strikes a balance between actuation force and deformation levels. MFCs comprise PZT fibers and epoxy with interdigitated electrodes embedded in a Kapton film (figure 1), yielding robustness and flexibility. The use of rectangular fiber cross-section provides good contact with the interdigitated electrodes (as compared to the previous generation called the active fiber composites with PZT fibers of circular cross section [51]). MFCs exploit the 33-mode of piezoelectricity (i.e., strain and electric field directions are identical) yielding an enhanced coupling coefficient (as compared to the standard flexural 31-mode of piezoelectricity). To leverage these characteristics, Ming *et al* [52] and Erturk and Delporte [53] developed MFC-based fins and explored their tethered swimming and thrust generation performance, respectively. Bimorph design (two piezoelectric laminates with a substrate driven out of phase) was employed in [53] to create bending motion.

As mentioned previously, piezoelectric actuators were not commonly used in fish-like robotics due to their high stress–low strain characteristics, requiring motion amplification mechanisms [46–48], as reported in a review article by Chu *et al* [6] in 2012. Shortly after that, to the best of our knowledge, the first untethered proof-of-concept piezoelectric swimmer was presented by Cen and Erturk [54] in 2013, with a design that consisted of a main body (not streamlined) housing the batteries and electronics, connected to a piezoelectric MFC bimorph fin. In a subsequent body of theoretical and experimental studies, we explored the linearized in vacuo structural dynamics [55] and underwater electrohydroelastic vibrations [56] of MFC bimorph cantilevers, as well as geometrically and materially nonlinear dynamics of around the fundamental bending mode for both actuation [57] and energy harvesting [58] in air. Underwater energy harvesting from translational and rotational base excitation of piezoelectric fins was explored by Erturk and Delporte [53] and Cha *et al* [59], respectively. Most recently, we have developed our second generation design [60, 61], with substantial enhancements compared to the aforementioned first generation effort [54], leading to a truly bioinspired concept that is subject to a detailed experimental investigation in the current work.

In the following, we present an experimental investigation of a trout-like multifunctional piezoelectric robotic fish design, which can also be used as an energy harvester. First, the design and manufacturing aspects are discussed in detail, which is followed by the experimental characterization of swimming speed in quiescent water (in a water tank) and under imposed flow (in a water tunnel). Hydrodynamic thrust frequency response is also discussed. Finally, energy harvesting results are summarized for a scenario in which the flexible tail was located in the wake of a cylindrical bluff body, with imposed

Figure 1. Detailed view of a single MFC laminate (M8514-P1 model is shown as an example) displaying piezoelectric fibers and interdigitated electrodes embedded in a Kapton film. Polyester electrode sheets (custom made by the manufacturer—Smart Material Corp.) enable waterproofing.

flow experiments conducted for a range of bluff body diameters and flow speeds.

2. Design and fabrication

The design of the robotic fish (figure 2) explored in this work was inspired by rainbow trout. The thrust-generating components of the design involve actively controllable MFCs bracketing a passive caudal fin, covering approximately one third of the main body, which is typical for subcarangiform and carangiform locomotion types [62] (trout locomotion is closer to subcarangiform). The rest of the fish body was divided into two additional parts, the nose and the body, where some space is reserved for electronics such as batteries and PCB high voltage amplifiers. Since the energy harvesting capabilities due to vortex-induced vibration are also of interest, the fish body was also designed to fit the necessary components for energy harvesting. In the following subsections, the design and manufacture of the fish are discussed in detail.
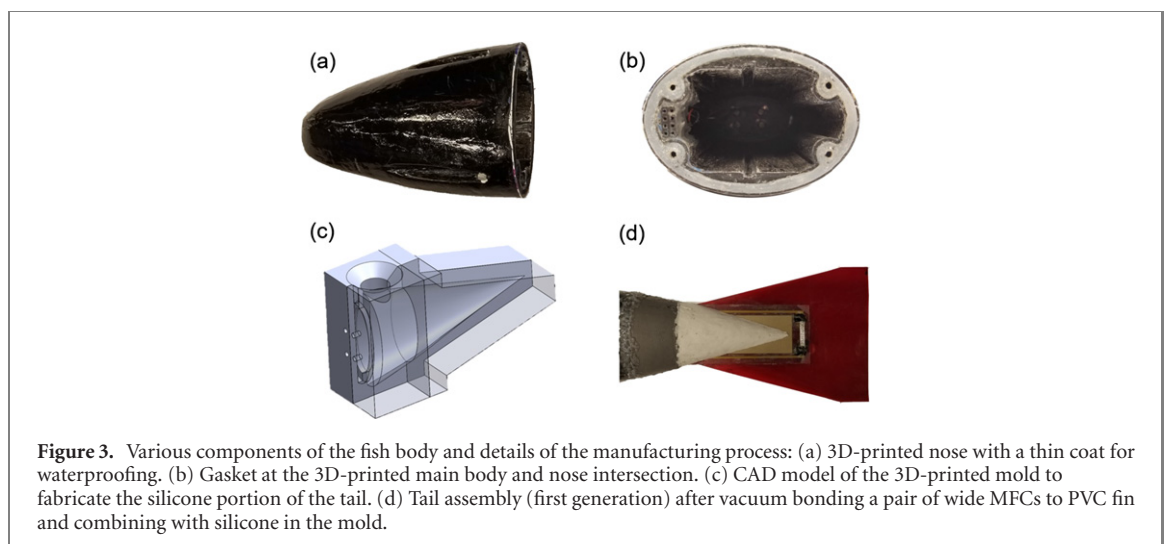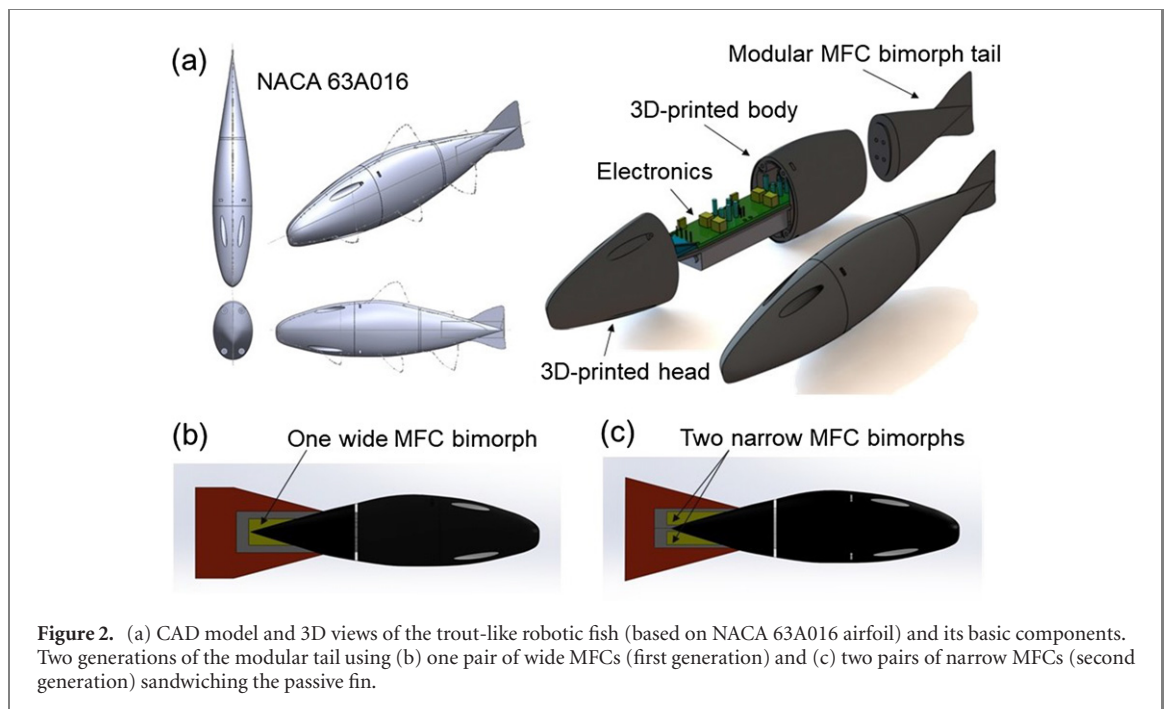
2.1. Design
The body shape of a trout is hydrodynamically similar to the NACA 63A016 airfoil [63]. The fish design here involves a 3.2 mm thick hollow shell in the form of this NACA airfoil for housing the electronics. Figure 2(a) shows 3D views of the robotic fish with reference sketches to illustrate the trout-like form of the design. The shell consists of three parts (the nose, the body, and the tail) and spans a total length of 30.5 cm. To secure the nose and the body together, four holes were added to the nose part for the attachment of 4–40

bolts and nuts. To waterproof the design, both the nose and the body feature a shallow 1.6 mm ridge to hold a gasket. Additionally, the tail portion features an embedded silicone flange that is compressed between two acrylic plates, providing a watertight seal as the tail is fastened onto the body with screws. The screws also provide electrical connection to the piezoelectric bimorph within the tail. The electronics inside the body are housed on two U-channels that allow for seamless sliding in and out of the body. The modular MFC tail can be replaced to study the effects of various fin shapes (which is of interest for future work). In the present study, only two tail configurations were explored in various parts of the paper: a first generation with two wide MFCs (M8528-P1 model with an active piezoelectric width of 28 mm in each MFC) and a second generation with four narrower MFCs (M8514-P1 model with an active piezoelectric width of 14 mm in each MFC), which are depicted in figures 2(b) and (c), respectively. Note that the second generation fin is intended for better authority in twisting and combined bending-twisting actuation, which is beyond the scope of the present work. Their overall performances in the context of this work (around the fundamental bending vibration mode) are similar and no comparison is intended. The initial design and swimming experiments were all based on the first generation fin, and we switched to the second generation in thrust estimation and power generation experiments.
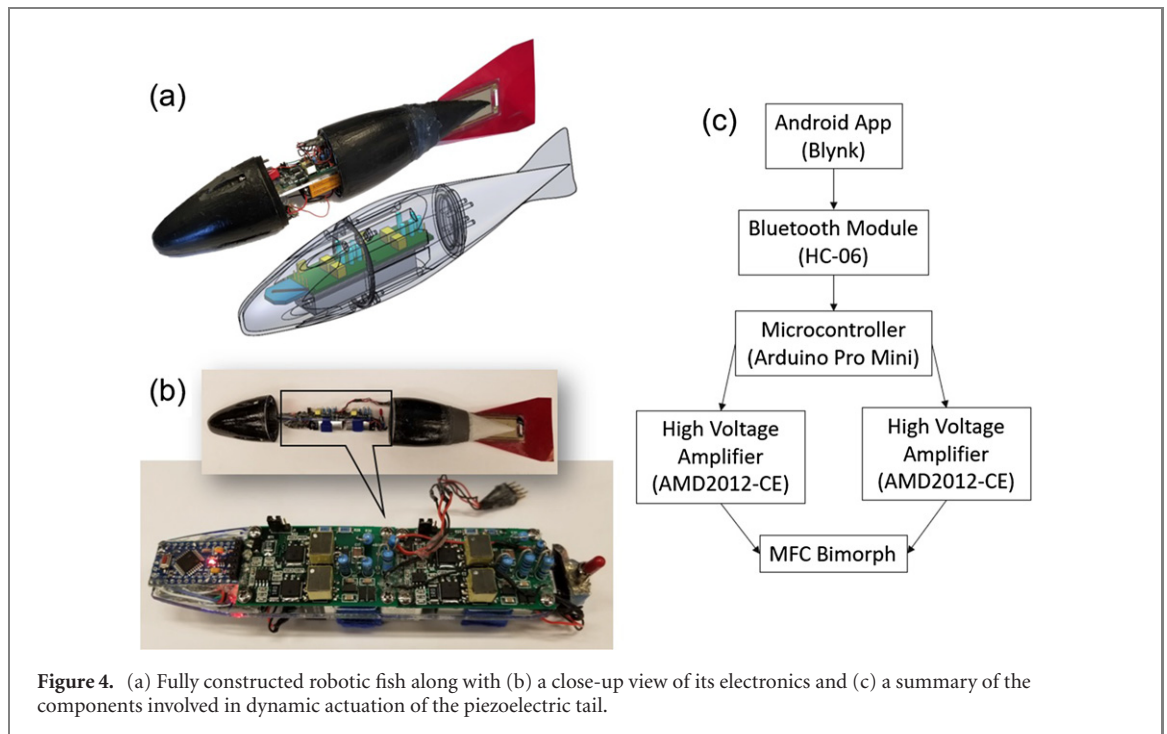
2.2. Manufacturing
Polylactic acid was used to 3D print the nose and the body. The layer lines on the exterior surfaces

Figure 2. (a) CAD model and 3D views of the trout-like robotic fish (based on NACA 63A016 airfoil) and its basic components. Two generations of the modular tail using (b) one pair of wide MFCs (first generation) and (c) two pairs of narrow MFCs (second generation) sandwiching the passive fin.

Figure 3. Various components of the fish body and details of the manufacturing process: (a) 3D-printed nose with a thin coat for waterproofing. (b) Gasket at the 3D-printed main body and nose intersection. (c) CAD model of the 3D-printed mold to fabricate the silicone portion of the tail. (d) Tail assembly (first generation) after vacuum bonding a pair of wide MFCs to PVC fin and combining with silicone in the mold.

were smoothed out with a thin coat of J-B Weld (figure 3(a)). To secure the nose and the body together, four 4–40 nuts were placed inside the body and fixed in place with J-B Weld. The nose was designed with four grooves such that bolts can freely slide in and engage with the nuts. The nose–body joint was waterproofed with a gasket (figure 3(b)) made by spraying mold release on the nose and filling in the groove between the nose and the body with silicone (GE silicone II). The two parts were then fastened together, and the silicone was allowed to cure overnight. Afterwards, the nose and the body were detached, leaving the gasket attached to the fish body. The nose and body were also sanded smooth, spray painted with a primer coat, a coat of plasti-dip, and two layers of a clear coat.

The flexible tail was made by vacuum bonding a pair of MFCs (M8528-P1) onto a 0.25 mm thick PVC (polyvinyl chloride) substrate using a high shear strength epoxy (3M DP-460). The flexible tapered section of the tail was made using a four-part mold (figure 3(c)). First the bimorph and the acrylic plate were placed inside the mold, after which a silicone mixture (Ecoflex 00-10 and glass microspheres to increase buoyancy) was poured in. This silicone tail was pressed into the body for water-proofing, and fastened with four 4–40 screws and a laser cut acrylic flange placed on the inside of the body. The assembled tail portion with the passive fin, MFC laminates, and the silicone is shown in figure 3(d). An electrical connection from the MFC tail to the electronics inside the body was established by attaching soldered wires from the MFC electrodes onto 4–40 nuts used for fastening the body and the tail. From the nuts, a soldered connection was created to a 4×2 female header strip placed near the nose–body joint for easy

Figure 4. (a) Fully constructed robotic fish along with (b) a close-up view of its electronics and (c) a summary of the components involved in dynamic actuation of the piezoelectric tail.

connection to the MFC. The wiring on the header strip was created such that flipping the orientation of the associated male header pins would only flip the direction of the fish without affecting its overall performance.

2.3. Electronics

Following the manufacturing procedure described in the previous section, the complete robotic fish was fabricated as shown in figure 4(a). The electronics were soldered together into a single compact unit and mounted onto a 3.2 mm thick laser cut acrylic base, letting the unit easily slide in and out of the fish body (figure 4(b)). The electronics unit is controlled by an Arduino Pro Mini using a mobile app (Blynk) connection established via a Bluetooth module (HC-06). With the app, commands can be sent to the microcontroller via virtual pins, allowing for precise control of the DC voltage, AC voltage amplitude, and the actuation frequency sent to each of the MFCs in the bimorph tail. The signals to the microcontroller were converted to an analog voltage output by sending a PWM signal through a low-pass filter into two high voltage amplifiers (AMD2012-CE3 from Smart Material Corp.) also attached to the electronics unit. These compact PCB high voltage amplifiers (suitable from DC to below 15 Hz) have a bilinear amplification scheme which maps to the -500 V to 1500 V voltage range of the MFCs. This process is summarized in figure 4(c). The high voltage amplifiers can be disabled with a digital on-off safety switch included in the software. Additionally, the electronics unit contains a 5 V and 12 V voltage regulator, two 9 V batteries, and a master kill switch. While the nose–body–tail gaskets and coats waterproof the

electronics by themselves, further caution was exercised by placing the electronics unit inside a ziplock bag. Finally, neodymium magnets were placed below the batteries for added mass to lower the center of gravity for stable swimming and to decrease the buoyancy of the fish.

3. Experimental characterization and results

Underwater locomotion and hydrodynamic thrust generation performance of the robotic fish was explored as discussed in the following subsections with representative results. The untethered swimmer can perform unconstrained locomotion via remote control through the app (described in the previous section), which is discussed in the following for small and large tank setups to identify the maximum swimming speed. Experiments were also conducted in a closed-loop water tunnel under imposed flow to confirm the maximum swimming speed and to estimate electrical power consumption. Thrust frequency response spanning the first three vibration modes was measured via quiescent water experiments. Finally, the tail portion of the robotic fish was used for energy harvesting from water flow in the wake of cylindrical bluff body samples with various diameters.

3.1. Swimming speed in quiescent water

The robotic fish was placed at the end of a small water tank of 99 cm length shown in figure 5(a). The fish was then allowed to reach a steady position in the water, after which the MFCs were actuated at various frequencies using a sinusoidal signal with 500 V DC offset and 1000 V AC amplitude (as per the voltage
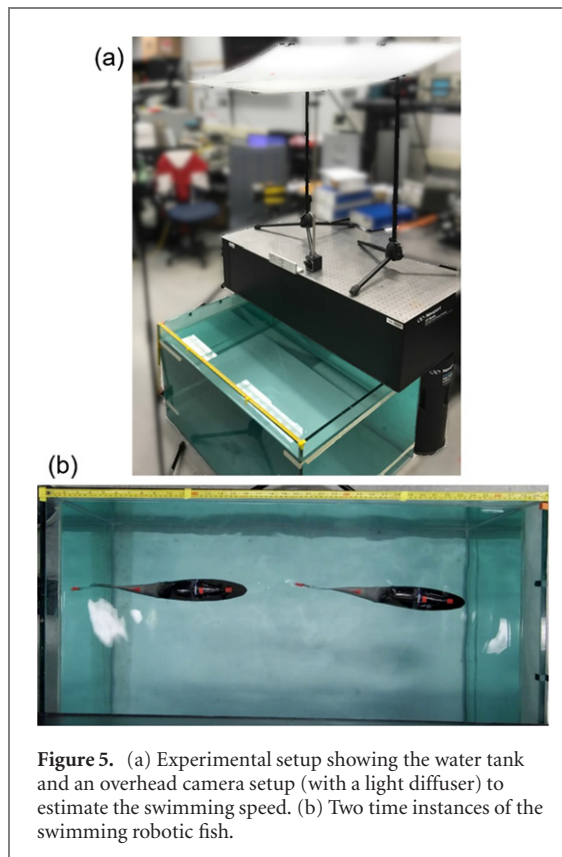
Figure 5. (a) Experimental setup showing the water tank and an overhead camera setup (with a light diffuser) to estimate the swimming speed. (b) Two time instances of the swimming robotic fish.

Figure 6. Sample displacement and normalized velocity versus time (a) in a small tank with limited space demonstrating acceleration from rest and (b) in a large water tank where the fish was allowed to reach steady-state velocity before entering the video frame.

range of MFCs provided by the manufacturer not to exceed the limits of -500 V and 1500 V), with the two sides of the bimorph actuated out of phase. Four red trackers were distributed along the length of the fish for velocity extraction via color-based object tracking. The trackers can be clearly seen in the top-down composite image of the fish in figure 5(b). Note the measuring tape on top of the composite image used for converting pixels to displacement.

MATLAB was used as the image processing and object tracking tool. The videos were imported and the length scale was converted from pixels to meters. The displacement for each of the four trackers relative to their distinct starting locations was tracked in time and differentiated to obtain the velocity. The two graphs in figure 6(a) show the average displacement and velocity (in terms of body length per second) across all trackers. Note that the displacement has a discontinuity slightly before 6 s. Here, the fish hit the back wall of the water tank and came to rest. The velocity here increases linearly with time, and presumably would have increased further in a larger water tank.

To capture the maximum speed of the robotic fish, more experiments were conducted in a larger water tank (in our underwater acoustics facilities), where the fish reached its full swimming potential. Video was recorded from the side due to the setup of the water tank facility. In this case, the fish was allowed to reach its steady-state swimming speed prior to entering the video frame. The known body
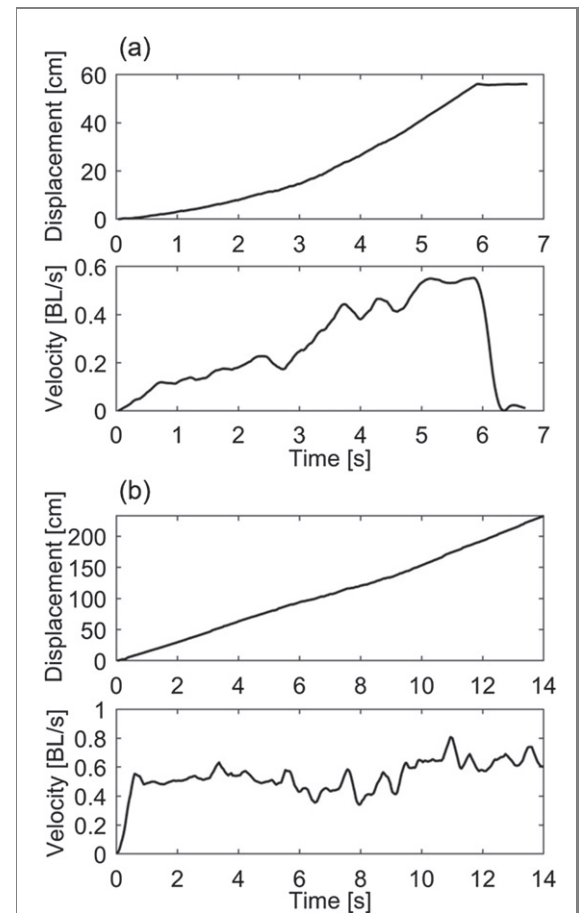
length of the fish was used for displacement conversion from pixels. The displacement and the velocity are then extracted using the object tracking process. Sample displacement and velocity data are shown in figure 6(b). The maximum instantaneous speed was 0.84 BL s^{-1} (body length per second), and the average speed from the entire video is 0.55 BL s^{-1}. This maximum unconstrained swimming speed was achieved for an actuation frequency of 5.6 Hz. Further experiments were conducted in this large tank for more complex actuation patterns. One such experiment was combination of resonant AC actuation bursts combined with gliding to one side with DC curvature for maneuvering as displayed in figure 7 [see the video in the supplementary document (https://stacks.iop.org/BB/16/046024/mmedia)].

3.2. Swimming speed under imposed flow

Next, the swimming performance of the robotic fish under imposed flow was measured. An ELD Inc. water tunnel with test section dimensions of 15.24 cm × 15.24 cm × 45.72 cm and a maximum flow speed of 1 m s^{-1} was used as the test-

Figure 7. Time instances of the robotic fish swimming in a large water tank with a demonstration of maneuvering via combination of bursts of AC actuation and gliding with DC actuation.

ing apparatus (figure 8(a)). This setup enables testing both untethered (battery powered) and tethered configurations, with the latter facilitating electrical power consumption analysis. The untethered fish was placed inside the test section and the flow speed was increased until the actuated fish remained stationary within the section. Fishing line kept the fish centered along the span-wise direction and an actuation frequency sweep was performed. In figure 8(b), the steady-state swimming speed is plotted against the tail actuation frequency. In the untethered configuration, the resonance was observed at 5.4 Hz with a maximum swimming speed of 0.71 BL s^{-1}. To measure the electrical power consumption as additional data, the robotic fish was tethered to a pair of high voltage amplifiers (Trek PA05039). Remarkably, not relying on the compact electronics of the robotic fish (figure 4(b)) and battery-powered PCB amplifier in dynamic actuation resulted in an enhanced swimming speed that reached 0.92 BL s^{-1} at the same resonance frequency of 5.4 Hz. From the actuation voltage and current data of the tethered setup, the average electrical power for the two high voltage amplifiers used for powering the fish was calculated as 250 mW.

Note that the maximum untethered swimming speed under imposed flow (0.71 BL s^{-1}) is lower than the maximum speed in quiescent water (0.84 BL s^{-1}). The difference can be attributed to the small test section and the resulting wall effects. Additionally, especially in the water tunnel setup, the robotic fish swims very close to the surface, as an additional source of deviation from the performance of an ideal swimmer setting submersed in a sufficient depth level.

3.3. Hydrodynamic thrust frequency response

We also investigated unidirectional thrust generation in a quiescent water setting and here we present representative results for the second-generation fin design. This fin differs from the first-generation design in that it uses two pairs of narrower MFCs (instead of a single wide MFC pair) as previously described with figure 2(c); however, the overall trends are similar since the focus in the current work is placed on unidirectional thrust using the fundamental bending mode (that produces straight swimming in AC

actuation). In the mean thrust measurement experiments, the nose part was removed and the remaining fish body was mounted to a calibrated cantilever as shown in figures 9(a)–(c). Lateral tail vibration was measured by a polytec laser Doppler vibrometer (LDV) while the constrained head displacement was measured using a Micro-Epsilon displacement sensor seen in figure 9(a). This thrust measurement method is based on our previous efforts [53, 54] to relate the cantilever mean displacement (constrained head displacement) to mean thrust. Briefly, prior to MFC actuation experiments, the vertical cantilever was calibrated for its quasi-static linear force–displacement relationship at the position where the robotic fish was attached and constrained displacement was measured by the laser sensor, the mean value of which was then converted to mean thrust. More information on this procedure can be found elsewhere [53, 54, 64].

Mean thrust frequency response is shown for different actuation voltage levels in figure 9(d) for a frequency range covering the first three vibration modes of the piezoelectric fin (see the supplementary document for an animation of these mode shapes). The linear (small amplitude) frequencies of these three modes are 2.7 Hz, 5.7 Hz, and 12 Hz. The focus in the present work is placed on the first bending mode around 2 Hz for the highest actuation voltage. Note that the resonance frequency decreases with increased actuation voltage, starting from a linear resonance at 2.7 Hz for low voltages—this is due to both piezoelectric softening nonlinearity [57, 58] and hydrodynamic nonlinearity with increased inertia coefficient, i.e., amplitude-dependent added mass [65, 66]. It should also be noted that this resonance frequency is not necessarily the full body's unconstrained locomotion resonance frequency, since the overall structure and boundary conditions are different in swimming experiments. The results in this subsection are mainly to estimate the thrust generation capability of the piezoelectric fin (yielding 20 mN or more), which compares well with biological fish of similar dimensions [67] and remarkably with Webb's early work [68, 69] reporting thrust levels for different swimming speeds in trout (he reported [68] 2435 dynes—or 24 mN—thrust for 23.6 cm s^{-1} swimming speed of a 30 cm rainbow trout, i.e., 0.79 BL s^{-1}, in agreement with the swimming speed in the previous section). The fundamental resonance frequency of the tail itself as well as the overall fish resonance in unconstrained locomotion in our work are also in agreement with the frequencies in [68]. Finally, it is remarkable to observe not only a twisting mode (mode 2) but also a more complex mode (mode 3) that can be very powerful in propulsion generation (with thrust levels as high as 80 mN) and it appears to be similar to the 'cupping' motion in the work by Esposito *et al* [70]. It is of interest to explore such complex 3D motions via multiple MFC
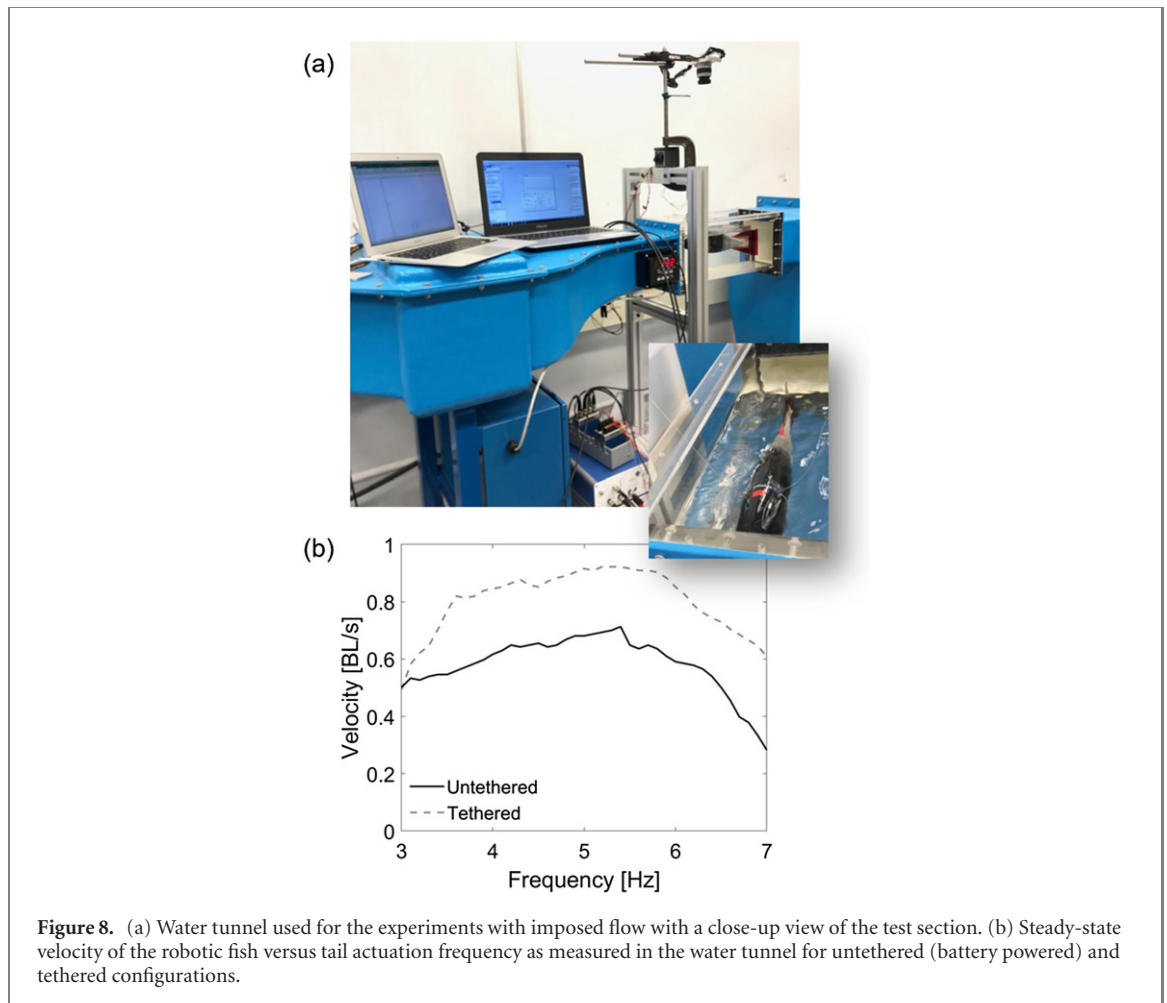
Figure 8. (a) Water tunnel used for the experiments with imposed flow with a close-up view of the test section. (b) Steady-state velocity of the robotic fish versus tail actuation frequency as measured in the water tunnel for untethered (battery powered) and tethered configurations.

patches (for more effective actuation authority) in the near future.

3.4. Flow energy harvesting

Next, the robotic fish was employed in a reverse manner to generate electricity from flow-induced vibration, as a demonstration of its multifunctional capability (which could readily be extended to sensing as well). Piezoelectricity is a reversible (two-way coupled) process, and therefore low-power electricity can be extracted in response to mechanical excitation of a piezoelectric device [71]. Piezoelectric energy harvesting has been heavily researched [72, 73] over the past two decades to convert structural vibrations into electricity and thereby to power small electronic components, such as wireless sensor nodes in passive and active monitoring applications. In most scenarios, direct vibrational or motion energy is available. However, in some cases, rather than direct structural motion, steady or unsteady fluid flow is available, which can be converted into electricity via energy harvester configurations employing various fluid–structure interaction concepts, such as the classical flutter via airfoils [74, 75] and hydrofoils [76], flag-like [77, 78] and inverted flag-like [79] settings exhibiting limit-cycle oscillations, bluff body wake and vortex-induced vibrations [80, 81],

among others. In the following, we consider energy harvesting from the inverted fish tail in the wake of a cylindrical bluff body (with different diameters). This configuration would correspond to the swimmer resting behind a bluff body in reverse position to harvest energy from shed vortices (i.e. it is not intended to emulate harvesting during locomotion).

In the energy harvesting setup, we continued with the second generation fin and employed parallel connection of the electrical outputs (one has the options to combine the piezoelectric laminates in series or parallel, for higher voltage or current, respectively). Typically, in piezoelectric transduction, the voltage output is high (enough to charge typical storage components) but the current levels are low, therefore it is reasonable to proceed with parallel connection in most applications involving multiple piezoelectric patches. The setup uses the portion without the nose as in thrust measurement experiments. The robotic fish was positioned in the test section of the water tunnel using a vertical bar attachment clamped to an external frame (figure 10(a)). The fish was positioned in the reverse configuration as compared to figure 8(a) to have the tail tip as the leading edge. A cylindrical bluff body was placed upstream. Four different bluff body diameters (28.6 mm, 25.4 mm, 15.9 mm, 9.5 mm) were explored (figure 10(b)). Adjustable
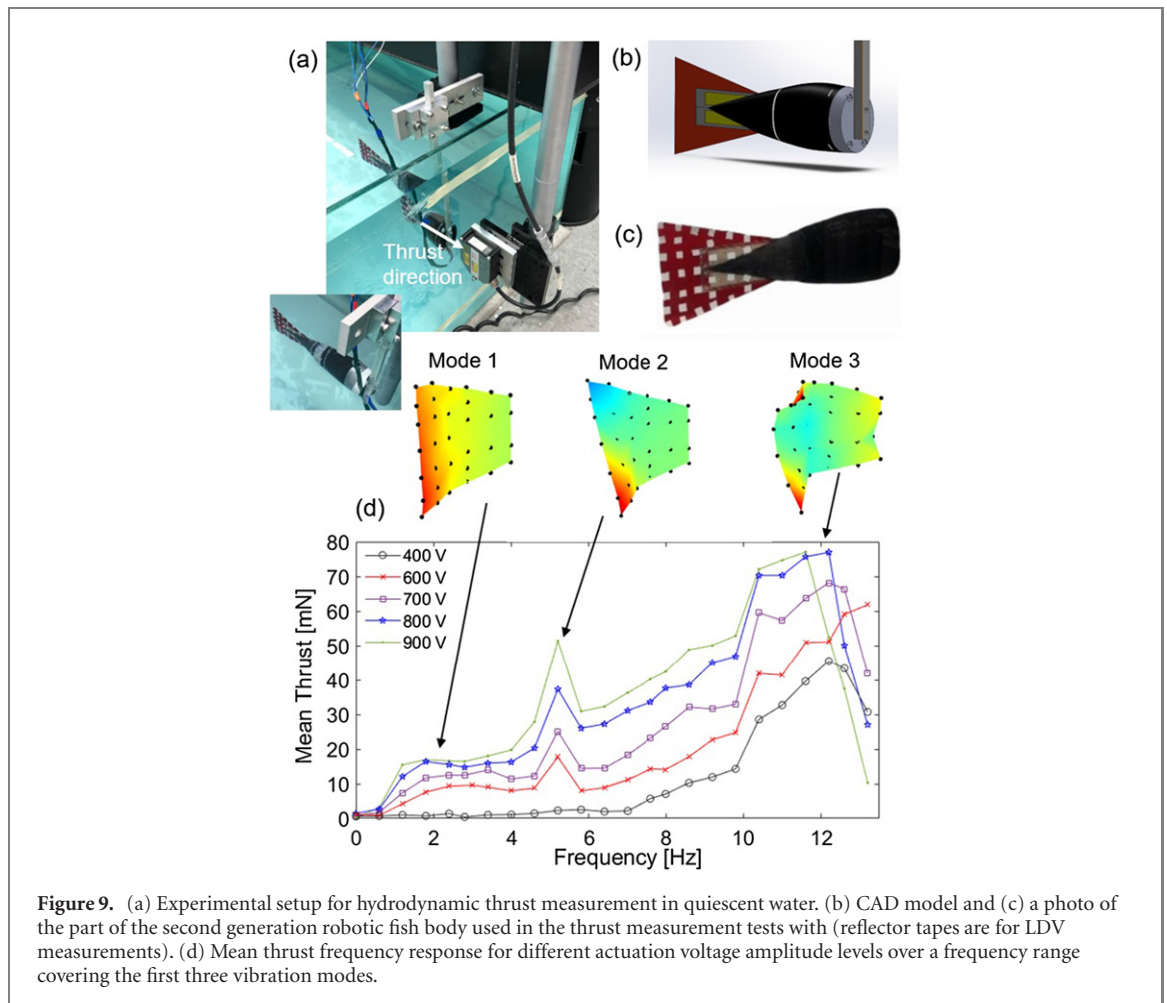
Figure 9. (a) Experimental setup for hydrodynamic thrust measurement in quiescent water. (b) CAD model and (c) a photo of the part of the second generation robotic fish body used in the thrust measurement tests with (reflector tapes are for LDV measurements). (d) Mean thrust frequency response for different actuation voltage amplitude levels over a frequency range covering the first three vibration modes.

resistance boxes were used as external loading for real electrical power measurement. An LDV measured the velocity signal at varying positions on the fin, from which the dominant excitation frequency at a given flow speed was extracted to confirm the shed vortex frequency.

First, the shed vortex frequency and flow speed relationship was investigated by varying the flow speed in each bluff body case and exploring the frequency content of the fish tail response (figure 11(a)). The vortex shedding frequency can be approximated by $f = \mathrm{St}\frac{U}{d_0}$ where U is the imposed flow speed, d_0 is the bluff body diameter, and St is the Strouhal number. The Strouhal number, St, is a function of the Reynolds number, Re; however, for $300 < \mathrm{Re} < 20{,}000$, $\mathrm{St} = 0.2$ is a good approximation. The experiments conducted here were in this Re regime, and figure 11(b) shows that the vortex shedding frequency for each cylinder indeed falls on the line with $\mathrm{St} = 0.2$.

It is known that the distance between the bluff body and the tail tip can be important as far as the harvested power is concerned. This distance was previously investigated by others (e.g., Akaydin *et al* [81] in air) and found to be around 2–$2.5d_0$. A preliminary set of experiments was conducted with a bluff body of $d_0 = 25.4$ mm by varying the distance (d) between the
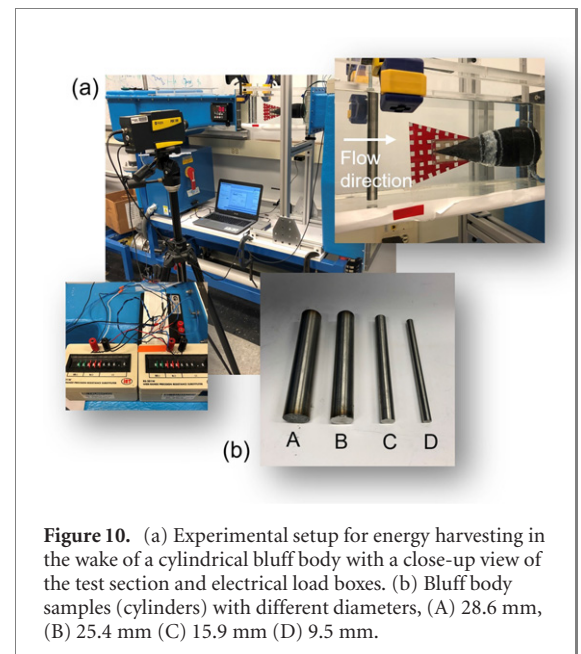

Figure 10. (a) Experimental setup for energy harvesting in the wake of a cylindrical bluff body with a close-up view of the test section and electrical load boxes. (b) Bluff body samples (cylinders) with different diameters, (A) 28.6 mm, (B) 25.4 mm (C) 15.9 mm (D) 9.5 mm.

center of the cylinder and the leading edge of the fin (i.e., tail tip), resulting in a similar finding here with $d = 2.5d_0$ yielding larger power (compared to $d = 2d_0$ and $d = 3d_0$). Next, resistor sweep experiments were performed for different cylinder diameters with
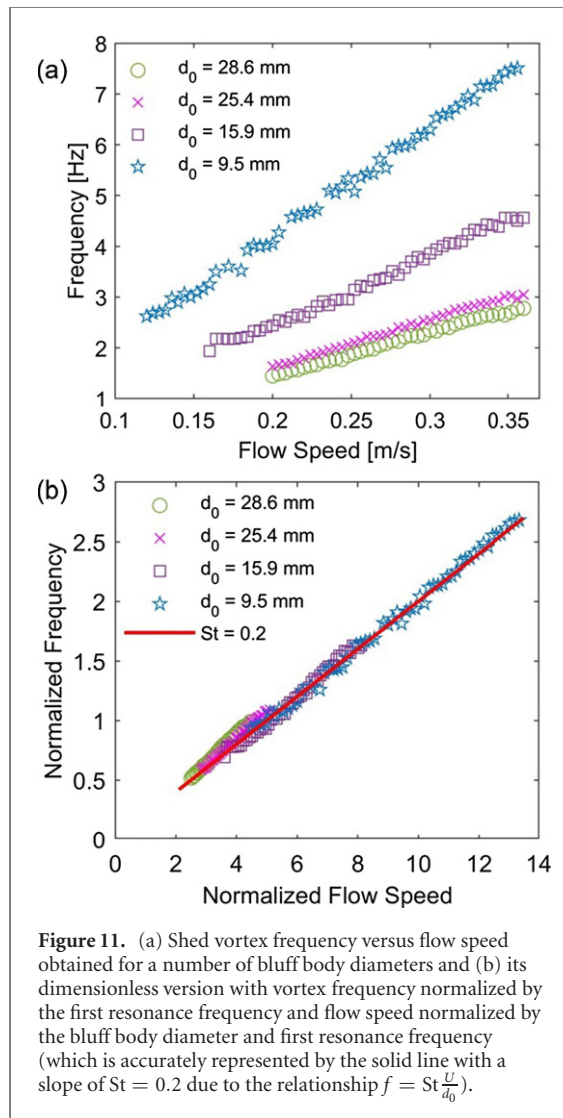
Figure 11. (a) Shed vortex frequency versus flow speed obtained for a number of bluff body diameters and (b) its dimensionless version with vortex frequency normalized by the first resonance frequency and flow speed normalized by the bluff body diameter and first resonance frequency (which is accurately represented by the solid line with a slope of St = 0.2 due to the relationship $f = \mathrm{St}\frac{U}{d_0}$).

Figure 12. Average electrical power versus load resistance and flow speed for a bluff body diameter of (a) $d_0 = 25.4$ mm and (b) $d_0 = 15.9$ mm ($d = 2.5d_0$ was used in each case for the distance between the center of the bluff body and the tail tip).

$d = 2.5d_0$ for each cylinder case. A set of resistive loads was tested for various flow speeds to cover the optimal load (which can be estimated at a given shed vortex frequency using the first-order circuit optimal load expression $R_{\mathrm{opt}} = \frac{1}{\omega C_{\mathrm{p}}}$ where C_{p} is the equivalent capacitance of the piezoelectric fin—this expression is suitable in a weakly coupled or highly damped energy harvester setting [71]—the latter is the case here). Two example plots are shown in figure 12 for the 25.4 mm and 15.9 mm cylinders, with peak powers approximately at 2.8 Hz and 2.9 Hz, respectively, which is the fundamental resonance (cf figure 9(d)). Therefore, the maximum power output is extracted when the shed vortex frequency hits this most flexible vibration mode (first mode) of the tail. At their respective optimal loads, the maximum power output obtained with the larger diameter cylinder is substantially larger even when each case independently had the corresponding optimal spacing ($d = 2.5d_0$) for their respective diameters, as a result of larger tip deflection (a representative video is provided in the supplementary document).
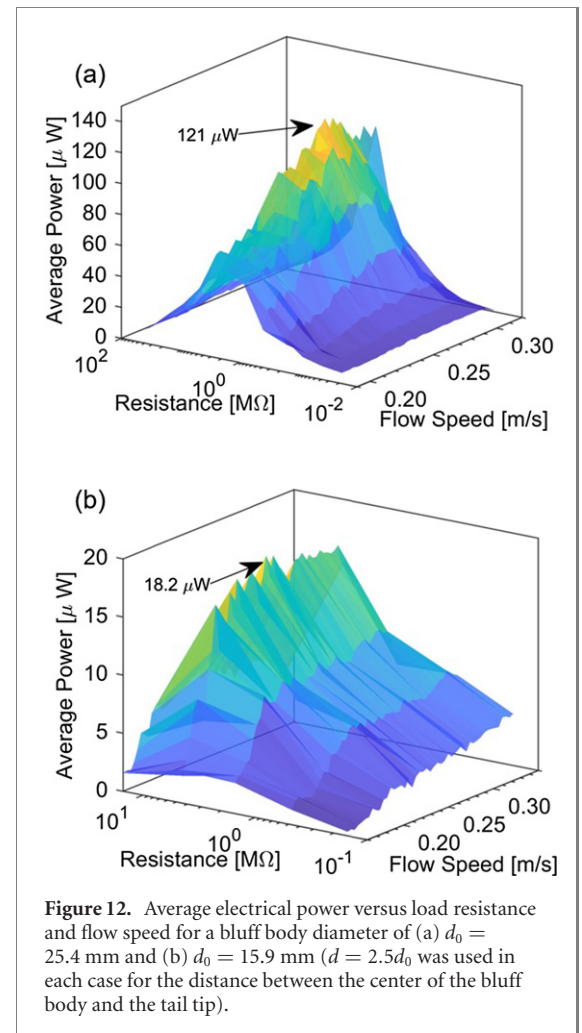
Finally, the distance between the center of each cylinder and the tail tip was kept constant (at $d = 60$ mm) and flow speed was varied for each of the four cylinders. Varying the flow speed changes the shed vortex frequency, which affects the optimal electrical load. In this case, the electrical load was adjusted to the respective optimal values and figure 13(a) was obtained for the average electrical power curves. When the horizontal axis is expressed in terms of the shed vortex frequency (according to figure 11), figure 13(b) is obtained. In this overall comparison for four different bluff body diameters, the maximum power is obtained for the flow speed with shed vortex frequency exciting the first mode (cf figures 9 and 13(b)).

It is worth noting that this sort of scenario would be intended for the swimmer resting behind a bluff body to harvest energy from shed vortices. While the harvested power is much lower than the power consumption in locomotion, such low-power electricity could be directly used to power small sensors (e.g. in ecological monitoring). Beyond that, if the swimmer rests in such a vortex field long enough, it may harvest enough energy to store and use in a short-term swimming mission for relocation.
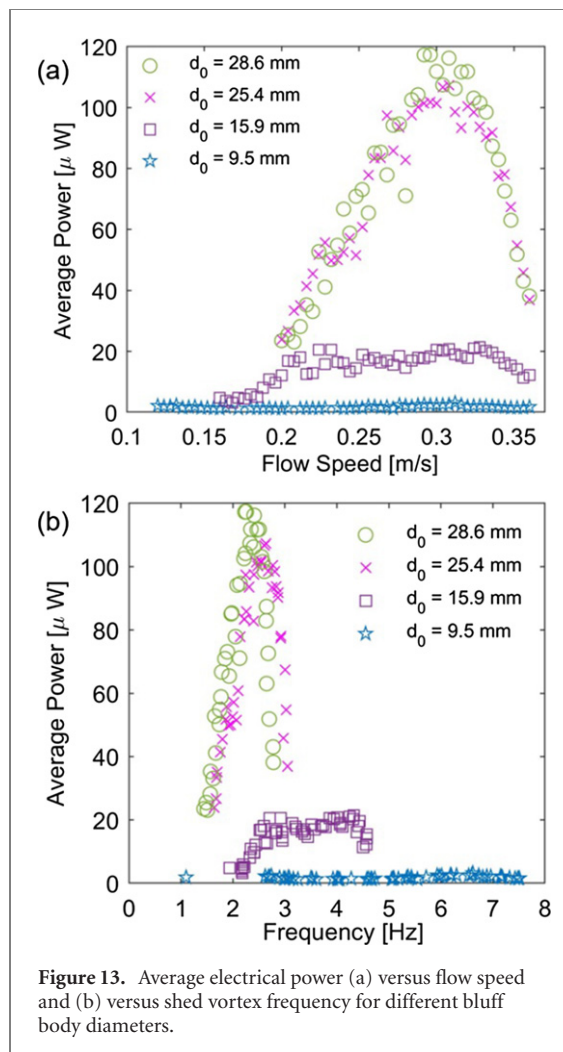
Figure 13. Average electrical power (a) versus flow speed and (b) versus shed vortex frequency for different bluff body diameters.

Figure 14. Performance comparison of smart material-based and motor-based untethered robotic fish. Current generation swimmer is at the intersection of these actuators, offering both geometric scalability and high performance.

4. Conclusion

In this work, a trout-like robotic swimmer and energy harvester was presented and experimentally characterized. MFC piezoelectric laminates were used as the actuator and energy harvester interface. MFCs are much more flexible than ordinary monolithic piezoelectric ceramics, yielding large deformation, but at the same time they preserve large force levels, striking the balance needed for effective hydrodynamic propulsion under resonant actuation. The prototype presented here generates thrust levels higher than other smart material-based concepts (e.g., ionic polymer–metal composites, IMPCs), while offering a simple design, ease of fabrication, geometric scalability, and silent operation unlike large scale robotic fish (e.g., motor-based configurations).

Swimming performance of the robotic fish was characterized in both quiescent water and under imposed flow, where the maximum speed was measured as 0.84 BL s^{-1} (body length per second) and 0.71 BL s^{-1}, respectively. Not surprisingly, a review of the literature of bio-inspired untethered robotic fish places the current work at the intersection of smart material-based and motor-based robotic
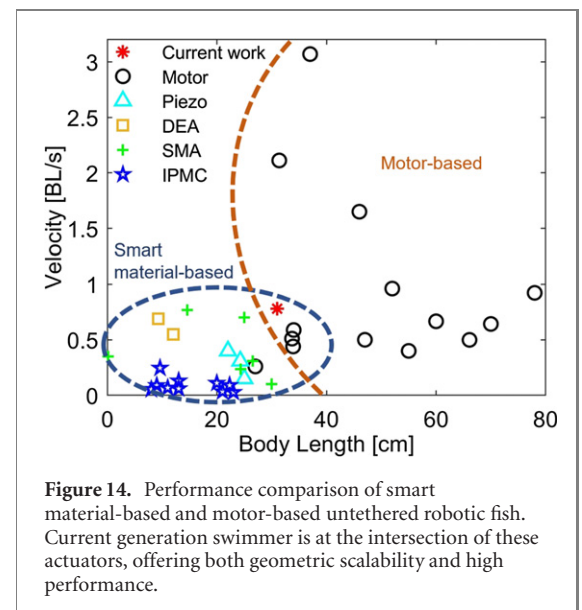
fish (figure 14), as the proposed design exhibits the advantages of both domains. The piezoelectric robotic fish presented in this work uses simple components such as bonded MFCs bracketing a passive fin, acting like artificial muscles, expanding and contracting in response to resonant actuation to produce bending motion. Therefore, unlike monolithic piezoelectrics, MFCs do not require motion amplification mechanisms; and unlike motor-based designs, there are no complex gear trains and joints to transmit the actuation power for propulsion. MFCs can easily be scaled down to enable small swimmers without manufacturing complexity, but they can also be scaled up to use in conjunction with large fins, in both cases without compromising on high performance and simplicity without bulky components.

The robotic fish platform presented in this work was also employed in flow energy harvesting in the wake of a cylindrical bluff body as a demonstration of its multifunctionality since piezoelectricity is a reversible process. Different bluff body diameters were explored over a range of flow speeds in a water tunnel test section where the fish body was reversed to locate the tail tip in the wake as the leading edge. Shed vortex frequency and flow speed relationship was well predicted by a Strouhal number of 0.2. It was observed that the maximum power output was obtained for flow speeds that yielded shed vortex frequencies around the fundamental (first bending mode) resonance frequency. This corresponded to around 2.8–2.9 Hz, while linear actuation resonance was obtained as 2.7 Hz. The maximum harvested power was 120 μW for a flow speed of 0.3 m s^{-1}. Such a power level could be sufficient in certain wireless sensing applications of the robotic fish (e.g., in ecological monitoring).

Finally, the fundamental resonance frequency neighborhood as well as thrust levels corresponding to the maximum swimming speed in this work agree well with those of the biological counterpart. Thrust levels on the order of tens of mN were easily achieved by the proposed design. Future efforts include efficiency measurement and analysis, as well as improvement via optimized fin design. It is worth mentioning that more intriguing vibration modes were observed with complex 3D deformations (yielding as high as 80 mN thrust), which can be actuated even more effectively with multiple MFC patches. Such concepts beyond imitating biological counterparts may open new avenues in robotic fish locomotion, which is of interest for future work.

Acknowledgments

Data availability statement

The data that support the findings of this study are available upon reasonable request from the authors.

ORCID iDs

Alper Erturk https://orcid.org/0000-0003-0110-5376

References

[1] Du R, Li Z, Youcef-Toumi K and Alvarado P V y 2015 *Robot Fish: Bio-Inspired Fishlike Underwater Robots* (Berlin: Springer)

[2] Katzschmann R K, DelPreto J, MacCurdy R and Rus D 2018 Exploration of underwater life with an acoustically controlled soft robotic fish *Sci. Robot.* **3** eaar3449

[3] Aureli M, Fiorilli F and Porfiri M 2012 Portraits of self-organization in fish schools interacting with robots *Physica* D **241** 908–20

[4] Bandyopadhyay P R 2005 Trends in biorobotic autonomous undersea vehicles *IEEE J. Oceanic Eng.* **30** 109–39

[5] Roper D T, Sharma S, Sutton R and Culverhouse P 2011 A review of developments towards biologically inspired propulsion systems for autonomous underwater vehicles *Proc. IMechE* **225** 77–96

[6] Chu W-S *et al* 2012 Review of biomimetic underwater robots using smart actuators *Int. J. Precis. Eng. Manuf.* **13** 1281–92

[7] Triantafyllou M S and Triantafyllou G S 1995 An efficient swimming machine *Sci. Am.* **272** 64–70

[8] Triantafyllou M S, Triantafyllou G S and Yue D K P 2000 Hydrodynamics of fishlike swimming *Annu. Rev. Fluid Mech.* **32** 33–53

[9] Barrett D S, Triantafyllou M S, Yue D K P, MA G and Wolfgang M J 1999 Drag reduction in fish-like locomotion *J. Fluid Mech.* **392** 183–212

[10] Hirata K *et al* 2000 Development of experimental fish robot *Proc. of the 6th Int. Symp. Marine Engineering (ISME 2000)* pp 23–7

[11] Fan R, Yu J, Wang L, Xie G, Fang Y and Hu Y 2005 Optimized design and implementation of biomimetic robotic dolphin *IEEE Int. Conf. on Robotics and Biomimetics-ROBIO* (IEEE) pp 484–9

[12] Low K H and Chong C W 2010 Parametric study of the swimming performance of a fish robot propelled by a flexible caudal fin *Bioinspiration Biomimetics* **5** 046002

[13] Wen L, Wang T, Wu G and Liang J 2012 Quantitative thrust efficiency of a self-propulsive robotic fish: experimental method and hydrodynamic investigation *IEEE/ASME Trans. Mechatronics* **18** 1027–38

[14] Yu J, Zhang C and Liu L 2016 Design and control of a single-motor-actuated robotic fish capable of fast swimming and maneuverability *IEEE/ASME Trans. Mechatronics* **21** 1711–9

[15] Liao P, Zhang S and Sun D 2018 A dual caudal-fin miniature robotic fish with an integrated oscillation and jet propulsive mechanism *Bioinspiration Biomimetics* **13** 036007

[16] Xie F, Li Z, Ding Y, Zhong Y and Du R 2019 An experimental study on the fish body flapping patterns by using a biomimetic robot fish *IEEE Robot. Autom. Lett.* **5** 64–71

[17] Chen D, Wu Z, Dong H, Tan M and Yu J 2020 Exploration of swimming performance for a biomimetic multi-joint robotic fish with a compliant passive joint *Bioinspiration Biomimetics* **16** 026007

[18] Anderson J M and Chhabra N K 2002 Maneuvering and stability performance of a robotic tuna *Integr. Comparative Biol.* **42** 118–26

[19] Hirata K, Takimoto T and Tamura K 2000 Study on turning performance of a fish robot *First Int. Symp. on Aqua Bio-Mechanisms* pp 287–92

[20] Liu J-D and Hu H 2006 Biologically inspired behaviour design for autonomous robotic fish *Int. J. Autom. Comput.* **3** 336–47

[21] Shin D, Na S Y, Kim J Y and Baek S-J 2007 Fish robots for water pollution monitoring using ubiquitous sensor networks with sonar localization *Int. Conf. on Convergence Information Technology (ICCIT 2007)* (IEEE) pp 1298–303

[22] Shin D, Na S Y, Kim J Y and Baek S-J 2008 Fuzzy neural networks for obstacle pattern recognition and collision avoidance of fish robots *Soft Comput.* **12** 715–20

[23] Ding R, Yu J, Yang Q, Tan M and Zhang J 2009 CPG-based dynamics modeling and simulation for a biomimetic amphibious robot *IEEE Int. Conf. on Robotics and Biomimetics (ROBIO)* (IEEE) pp 1657–62

[24] Marchese A D, Onal C D and Rus D 2014 Autonomous soft robotic fish capable of escape maneuvers using fluidic elastomer actuators *Soft Robot.* **1** 75–87

[25] Du S, Wu Z and Yu J 2019 Design and yaw control of a two-motor-actuated biomimetic robotic fish *IEEE Int. Conf. on Robotics and Biomimetics (ROBIO)* (IEEE) pp 126–31

[26] Epps B P, Alvarado P V y, Youcef-Toumi K and Techet A H 2009 Swimming performance of a biomimetic compliant fish-like robot *Exp. Fluids* **47** 927–39

[27] Zhong Y, Li Z and Du R 2017 A novel robot fish with wire-driven active body and compliant tail *IEEE/ASME Trans. Mechatronics* **22** 1633–43

[28] Zhong Y, Song J, Yu H and Du R 2018 Toward a transform method from lighthill fish swimming model to biomimetic robot fish *IEEE Robot. Autom. Lett.* **3** 2632–9

[29] Leo D J 2007 *Engineering Analysis of Smart Material Systems* (New York: Wiley)

[30] Shahinpoor M 1992 Conceptual design, kinematics and dynamics of swimming robotic structures using ionic polymeric gel muscles *Smart Mater. Struct.* **1** 91

[31] Guo S, Fukuda T and Asaka K 2003 A new type of fish-like underwater microrobot *IEEE/ASME Trans. Mechatronics* **8** 136–41

[32] Kim B, Kim D-H, Jung J and Park J-O 2005 A biomimetic undulatory tadpole robot using ionic polymer–metal composite actuators *Smart Mater. Struct.* **14** 1579

[33] Tan X, Kim D, Usher N, Laboy D, Jackson J, Kapetanovic A, Rapai J, Sabadus B and Zhou X 2006 An autonomous robotic fish for mobile sensing *IEEE/RSJ Int. Conf. on Intelligent Robots and Systems* (IEEE) pp 5424–9

[34] Ye X, Su Y, Guo S and Wang L 2008 Design and realization of a remote control centimeter-scale robotic fish *IEEE/ASME Int. Conf. on Advanced Intelligent Mechatronics* (IEEE) pp 25–30

[35] Brunetto P, Fortuna L, Graziani S and Strazzeri S 2008 A model of ionic polymer–metal composite actuators in underwater operations *Smart Mater. Struct.* **17** 025029

[36] Mbemmo E, Chen Z, Shatara S and Tan X 2008 Modeling of biomimetic robotic fish propelled by an ionic polymer–metal composite actuator *IEEE Int. Conf. on Robotics and Automation* (IEEE) pp 689–94

[37] Chen Z, Shatara S and Tan X 2009 Modeling of biomimetic robotic fish propelled by an ionic polymer–metal composite caudal fin *IEEE/ASME Trans. Mechatronics* **15** 448–59

[38] Aureli M, Kopman V and Porfiri M 2009 Free-locomotion of underwater vehicles actuated by ionic polymer metal composites *IEEE/ASME Trans. Mechatronics* **15** 603–14

[39] Chen Z, Um T I and Bart-Smith H 2011 A novel fabrication of ionic polymer–metal composite membrane actuator capable of three-dimensional kinematic motions *Sensors Actuators* A **168** 131–9

[40] Shinjo N and Swain G W 2004 Use of a shape memory alloy for the design of an oscillatory propulsion system *IEEE J. Oceanic Eng.* **29** 750–5

[41] Wang Z, Hang G, Wang Y, Li J and Du W 2008 Embedded SMA wire actuated biomimetic fin: a module for biomimetic underwater propulsion *Smart Mater. Struct.* **17** 025039

[42] Wang Z, Wang Y, Li J and Hang G 2009 A micro biomimetic manta ray robot fish actuated by SMA *IEEE Int. Conf. on Robotics and Biomimetics (ROBIO)* (IEEE) pp 1809–13

[43] Rossi C, Colorado J, Coral W and Barrientos A 2011 Bending continuous structures with SMAs: a novel robotic fish design *Bioinspiration Biomimetics* **6** 045005

[44] Jin H, Dong E, Xu M, Liu C, Alici G and Jie Y 2016 Soft and smart modular structures actuated by shape memory alloy (SMA) wires as tentacles of soft robots *Smart Mater. Struct.* **25** 085026

[45] Shaw H and Thakur A 2019 Shape memory alloy based caudal fin for a robotic fish: design, fabrication, control and characterization *Proc. of the Advances in Robotics 2019* pp 1–6

[46] Fukuda T, Kawamoto A, Arai F and Matsuura H 1995 Steering mechanism and swimming experiment of micro mobile robot in water *Proc. IEEE Micro Electro Mechanical Systems* (IEEE) 300

[47] Heo S, Wiguna T, Park H C and Goo N S 2007 Effect of an artificial caudal fin on the performance of a biomimetic fish robot propelled by piezoelectric actuators *J. Bionic Eng.* **4** 151–8

[48] Wiguna T, Heo S, Park H C and Goo N S 2009 Design and experimental parameteric study of a fish robot actuated by piezoelectric actuators *J. Intell. Mater. Syst. Struct.* **20** 751–8

[49] Keats Wilkie W, Bryant R G, James W H, Fox R L, Hellbaum R F, Anthony J Jr, Little B D and Mirick P H 2000 Low-cost piezocomposite actuator for structural control applications *Smart Structures and Materials 2000: Industrial and Commercial Applications of Smart Structures Technologies*

[50] James W and Keats Wilkie W 2003 *Method of fabricating NASA-standard macro-fiber composite piezoelectric actuators* NASA/TM-2003-2 12427 NASA

[51] Bryant R G 2007 Overview of NASA Langley's piezoelectric ceramic packaging technology and applications Tokyo *10th Japan Int. SAMPE Symp. and Exhibition: JISSE-10*

[52] Ming A, Park S, Nagata Y and Shimojo M 2009 Development of underwater robots using piezoelectric fiber composite *IEEE Int. Conf. on Robotics and Automation* (IEEE) pp 3821–6

[53] Erturk A and Delporte G 2011 Underwater thrust and power generation using flexible piezoelectric composites: an experimental investigation toward self-powered swimmer-sensor platforms *Smart Mater. Struct.* **20** 125013

[54] Cen L and Erturk A 2013 Bio-inspired aquatic robotics by untethered piezohydroelastic actuation *Bioinspiration Biomimetics* **8** 016006

[55] Shahab S and Erturk A 2017 Coupling of experimentally validated electroelastic dynamics and mixing rules formulation for macro-fiber composite piezoelectric structures *J. Intell. Mater. Syst. Struct.* **28** 1575–88

[56] Shahab S and Erturk A 2016 Electrohydroelastic Euler–Bernoulli–Morison model for underwater resonant actuation of macro-fiber composite piezoelectric cantilevers *Smart Mater. Struct.* **25** 105007

[57] Tan D, Yavarow P and Erturk A 2018 Nonlinear elastodynamics of piezoelectric macro-fiber composites with interdigitated electrodes for resonant actuation *Compos. Struct.* **187** 137–43

[58] Tan D, Yavarow P and Erturk A 2018 Resonant nonlinearities of piezoelectric macro-fiber composite cantilevers with interdigitated electrodes in energy harvesting *Nonlinear Dyn.* **92** 1935–45

[59] Cha Y, Chae W, Kim H, Walcott H, Peterson S D and Porfiri M 2016 Energy harvesting from a piezoelectric biomimetic fish tail *Renew. Energy* **86** 449–58

[60] Tan D, Le Dault Y-A and Erturk A 2019 Characterization of a bio-inspired piezoelectric swimmer in a quiescent water and under imposed flow *Active and Passive Smart Structures and Integrated Systems XIII* vol 10967 (International Society for Optics and Photonics) 109670X

[61] Wang Y-C, Kohtanen E and Erturk A 2020 Characterization of a multifunctional bioinspired piezoelectric swimmer and energy harvester *ASME 2020 Conf. on Smart Materials, Adaptive Structures and Intelligent Systems* (American Society of Mechanical Engineers Digital Collection)

[62] Sfakiotakis M, Lane D M and Davies J B C 1999 Review of fish swimming modes for aquatic locomotion *IEEE J. Oceanic Eng.* **24** 237–52

[63] Azuma A 2006 *The Biokinetics of Flying and Swimming* 2nd edn (Reston, VA: American Institute of Aeronautics and Astronautics)

[64] Erturk A 2015 Macro-fiber composite actuated piezoelectric robotic fish *Robot Fish* (Berlin: Springer) pp 255–83

[65] Tan D and Erturk A 2018 On the coupling of nonlinear macro-fiber composite piezoelectric cantilever dynamics with hydrodynamic loads *Active and Passive Smart Structures and Integrated Systems XII* vol 10595 (International Society for Optics and Photonics) 105950R

[66] Demirer E, Wang Y-C, Erturk A and Alexander A 2020 Effect of actuation method on hydrodynamics of elastic plates oscillating at resonance *J. Fluid Mech.* **910** A4 (accepted)

[67] Lauder G V and Drucker E G 2002 Forces, fishes, and fluids: hydrodynamic mechanisms of aquatic locomotion *Physiology* **17** 235–40

[68] Webb P W 1971 The swimming energetics of trout *J. Exp. Biol.* **55** 489–520

[69] Webb P W 1971 The swimming energetics of trout *J. Exp. Biol.* **55** 521–40

[70] Esposito C J, Tangorra J L, Flammang B E and Lauder G V 2012 A robotic fish caudal fin: effects of stiffness and motor program on locomotor performance *J. Exp. Biol.* **215** 56–67

[71] Erturk A and Inman D J 2011 *Piezoelectric Energy Harvesting* (New York: Wiley)

[72] Anton S R and Sodano H A 2007 A review of power harvesting using piezoelectric materials (2003–2006) *Smart Mater. Struct.* **16** R1

[73] Safaei M, Sodano H A and Anton S R 2019 A review of energy harvesting using piezoelectric materials: state-of-the-art a decade later (2008–2018) *Smart Mater. Struct.* **28** 113001

[74] Erturk A, Vieira W G R, De Marqui C Jr and Inman D J 2010 On the energy harvesting potential of piezoaeroelastic systems *Appl. Phys. Lett.* **96** 184103

[75] Bryant M and Garcia E 2011 Modeling and testing of a novel aeroelastic flutter energy harvester *J. Vib. Acoust.* **133** 011010

[76] Akcabay D T and Young Y L 2012 Hydroelastic response and energy harvesting potential of flexible piezoelectric beams in viscous flow *Phys. Fluids* **24** 054106

[77] Michelin S and Doaré O 2013 Energy harvesting efficiency of piezoelectric flags in axial flows *J. Fluid Mech.* **714** 489–504

[78] De Marqui C Jr, Tan D and Erturk A 2018 On the electrode segmentation for piezoelectric energy harvesting from nonlinear limit cycle oscillations in axial flow *J. Fluids Struct.* **82** 492–504

[79] Orrego S, Shoele K, Ruas A, Doran K, Caggiano B, Mittal R and Kang S H 2017 Harvesting ambient wind energy with an inverted piezoelectric flag *Appl. Energy* **194** 212–22

[80] Allen J J and Smits A J 2001 Energy harvesting eel *J. Fluids Struct.* **15** 629–40

[81] Akaydın H D, Elvin N and Andreopoulos Y 2010 Wake of a cylinder: a paradigm for energy harvesting with piezoelectric materials *Exp. Fluids* **49** 291–304